JACS
JOURNAL OF THE AMERICAN CHEMICAL SOCIETY

Article

pubs.acs.org/JACS

Role of Edge Engineering in Photoconductivity of Graphene Nanoribbons

Ivan Ivanov,*[,†] Yunbin Hu,[†] Silvio Osella,[‡,§] Uliana Beser,[†] Hai I. Wang,[†,#] David Beljonne,[‡] Akimitsu Narita,[†] Klaus Müllen,[†] Dmitry Turchinovich,[†] and Mischa Bonn*[,†]

[†]Max Planck Institute for Polymer Research, Ackermannweg 10, 55128 Mainz, Germany

[‡]Laboratory for Chemistry of Novel Materials, University of Mons, Place du Parc 20, B-7000 Mons, Belgium

[§]Centre of New Technologies, University of Warsaw, Banacha 2c, 02-097 Warszawa, Poland

[#]Institute of Physics, Johannes Gutenberg-University Mainz, Staudingerweg 7, 55128 Mainz, Germany

ABSTRACT: The effect of edge engineering of graphene nanoribbons (GNRs) on their ultrafast photoconductivity is investigated. Three different GNRs were fabricated by bottom-up synthesis in the liquid phase, where structure, width, and edge planarity could be controlled chemically at the atomic level. The charge carrier transport in the fabricated GNRs was studied on the ultrafast, sub-picosecond time scale using time-resolved terahertz spectroscopy, giving access to the elementary parameters of carrier conduction. While the variation of the side chains does not alter the photoconductive properties of GNRs, the edge structure has a strong impact on the carrier mobility in GNRs by affecting the carrier momentum scattering rate. Calculations of the ribbon electronic structure and theoretical transport studies show that phonon scattering plays a significant role in microscopic conduction in GNRs with different edge structures. A comparison between theory and experiment indicates that the mean free path of charge carriers in the nanoribbons amounts to typically ~20 nm.

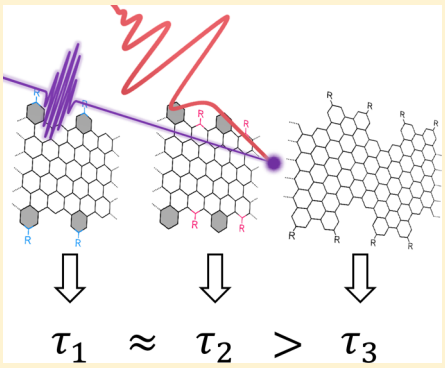

INTRODUCTION

Since its initial discovery,[1] graphene has been attracting much attention from both a scientific[2] and technological perspective.[3] Graphene is a unique two-dimensional, gapless material, whose electrons possess a linear energy-momentum dispersion over a large range of energies and momenta. Owing to its unique linear band structure, the charge carriers in graphene behave as massless particles, giving rise to exceptionally high dc charge carrier mobilities up to 350 000 $cm^2\ V^{-1}\ s^{-1}$.[4] Its gapless electronic band structure results in a broadband absorption spectrum,[5,6] making graphene advantageous for numerous applications. On the other hand, the gapless nature of graphene prohibits its applicability in the fields where a band gap is essential, such as photovoltaics[7] or logic transistors.[8,9] Nanometer-wide graphene structures, i.e., nanoribbons, undergo band-gap opening as a result of quantum confinement of electrons.[10] The fabrication of graphene nanoribbons (GNRs) has advanced tremendously in recent years, starting from the actual slicing of the graphene monolayer into GNRs using lithography[11,12] as well as unzipping of carbon nanotubes[13,14] and culminating in the chemical synthesis of GNRs by a bottom-up approach.[15−17] The latter is particularly appealing, as it allows chemically controlling a variety of properties of the GNRs and producing macroscopic quantities of structurally identical GNRs. This route provides the means for engineering GNRs, where, for instance, the width of a nanoribbon can be controlled with atomic precision, whereby the band gap and related optical properties can be tuned. Moreover, the edge structure and the orientation of the lattice can similarly be customized, providing a way toward predictable structure-related effects such as magnetoresistance in GNRs with zigzag edge morphology.[18] For the edge structure, in particular, the alkyl groups can be used to chemically functionalize the nanoribbons and control their interactions with specific solvents and surfaces. This in turn offers control over the solubility of the ribbons and, hence, their further solution processability into functional devices. All this makes GNRs a promising new class of electronic materials and renders it essential to obtain an understanding of microscopic electronic transport in GNRs.

Given the possibility of such an exquisite chemical control in these systems, an increasingly relevant question is, how exactly the structural features of the GNRs—the width, edge structure, and lattice orientation—affect their conductive properties. Here, we investigate ultrafast charge transport of photoinjected charge carriers in three types of graphene nanoribbons with different edge structures, lattice orientations, and different widths. We have studied the influence of structural modifications of the GNRs on the microscopic carrier transport, probed using ultrafast terahertz (THz) spectroscopy.

Received: April 6, 2017
Published: May 19, 2017

DOI: 10.1021/jacs.7b03467
J. Am. Chem. Soc. 2017, 139, 7982−7988

THz spectroscopy is used to interrogate the (photo)-conductive response of materials of interest in a contact-free fashion using a freely propagating pulse of far-infrared radiation. The ability to measure the conductivity without contacts makes this method particularly attractive to investigate the charge transport on the nanoscale,[19] where contact-based measurements are naturally challenging.[11,20−23] THz (photo)-conductivity spectra and their interpretation allow access to fine details of carrier transport in the systems of interest, such as the number density of conducting charge carriers, the free carrier lifetime, carrier momentum scattering time, and the mechanism of (photo)conductivity such as free versus bound charge and free charge localized on long-range potential corrugations.[24] The findings of this work, in particular, demonstrate that the conduction in GNRs with similar optical fingerprints is strongly dependent on the edge structure of the GNRs, while the side-chain modifications have very limited impact on carrier transport.

RESULTS AND DISCUSSION

The GNRs under study are prepared by a solution-based bottom-up protocol,[15] with edges that are typically functionalized by alkyl chains to enhance solubility.[25] The alkyl chains can be attached to different benzene rings at the GNR edge. For instance, the dodecyl chains ($C_{12}H_{25}$) can be bonded at the outermost "edge" or innermost "cove" sites of 6CGNR structure (the "cove"-type GNRs with six zigzag chains along the ribbon axis[26]) as shown in Figure 1a and b, respectively.[27]

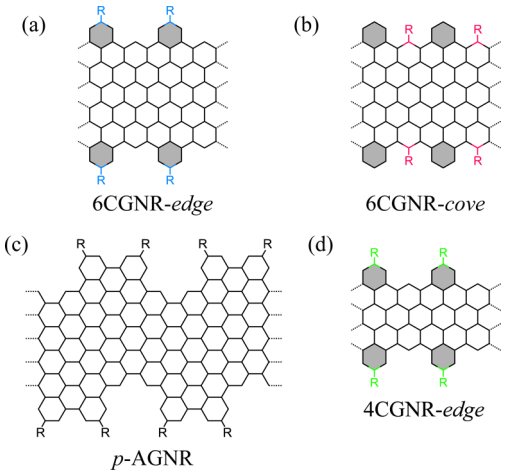

Figure 1. Chemical structure of the GNRs investigated in this work (a−c) as well as the one studied previously (d).[30] (a) 6CGNR-*edge*, with dodecyl ($C_{12}H_{15}$) chains on the outer benzene rings (shaded with gray), blue color. (b) 6CGNR-*cove* with chains on the inner benzene rings, red color. (c) *p*-AGNR terminated by the same dodecyl chains. (d) 4CGNR-*edge* investigated by Jensen et al.[30] Dodecyl chains are marked with R.

The precise position of the dodecyl chains affects the structure of 6CGNR: when sitting in the "cove" sites (see Figure 1b), they cause out-of-plane bending of neighboring protruding benzene rings (marked with gray in Figure 1b), while the 6CGNR structure with the chains attached to these protruding rings retains a planar geometry (Figure 1a). This structural distortion of the 6CGNR-*cove* causes the band-gap lowering in comparison to the 6CGNR-*edge* (the details of this will be published elsewhere[27]). The dependence of the band structure on the precise location of the alkyl chains is immediately apparent from the optical absorption spectra, as shown in Figure 2, where the absorption spectra of these two types of

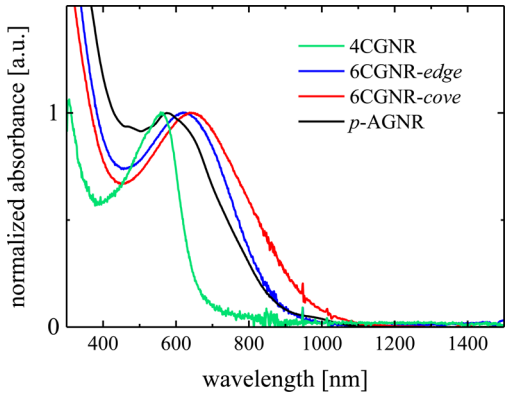

Figure 2. Absorbance of the investigated GNR samples dispersed in TCB solvent. The data have been normalized to the exciton resonance maxima of the GNRs.

6CGNR structures (blue and red lines in Figure 2, respectively) are compared. An important question thus arises: since the change in the edge planarity clearly affects the band structure, how does it influence the microscopic charge transport? Inversely, GNRs with seemingly very different edge morphology can have very similar optical properties. For example, the *p*-AGNR[26,28] structure (shown in Figure 1c), a GNR of similar width, but strongly curved edges, has optical properties very similar to both the edge and cove 6CGNRs (see Figure 2, black line). Again, the question regarding electronic transport properties presents itself.

In this work, we experimentally study the photoconductivity of the three GNRs: 6CGNR-*edge*, 6CGNR-*cove*, and *p*-AGNR (see Figure 1a, b, and c, respectively), which are typically hundreds of nanometers long.[15,16] All three GNR samples are dispersed in 1,2,4-trichlorobenzene (TCB). TCB is transparent at both optical and THz frequencies. The optical absorption spectra of the three GNRs in dispersion are shown in Figure 2, revealing that the optical band gaps of all samples are in the spectral range between 900 and 1000 nm. The optical spectra of all GNR samples are dominated by an optical transition of excitonic origin. For comparison, we also present the optical absorption spectrum of a narrower 4CGNR with a larger band gap (green line in Figure 2): its optical and conductive properties and band structure calculations have been presented previously elsewhere.[29,30]

In our optical pump−THz probe experiments, the GNRs are photoexcited using ultrashort (40 fs) optical laser pulses with 3.1 eV photon energy (400 nm wavelength). The energy of the excitation photons exceeds the band gap of all investigated nanoribbons (see Figure 2); therefore upon photoexcitation electron−hole pairs can be generated, in addition to excitons. The origin of the free charge carriers presumably lies in the dissociation of "hot" excitons, which is known to lead to free carrier formation at short delay times.[31] The observed lack of real conductivity following resonant excitation at 600 nm (data not shown) is consistent with this conclusion.

The photoconductivity response of these free carriers is then interrogated via freely propagating, ca. picosecond-long pulses of THz radiation. The transmission of the electromagnetic field of the probe THz pulses through the photoexcited GNR dispersion is measured directly in the time domain, at different

DOI: 10.1021/jacs.7b03467
J. Am. Chem. Soc. 2017, 139, 7982−7988

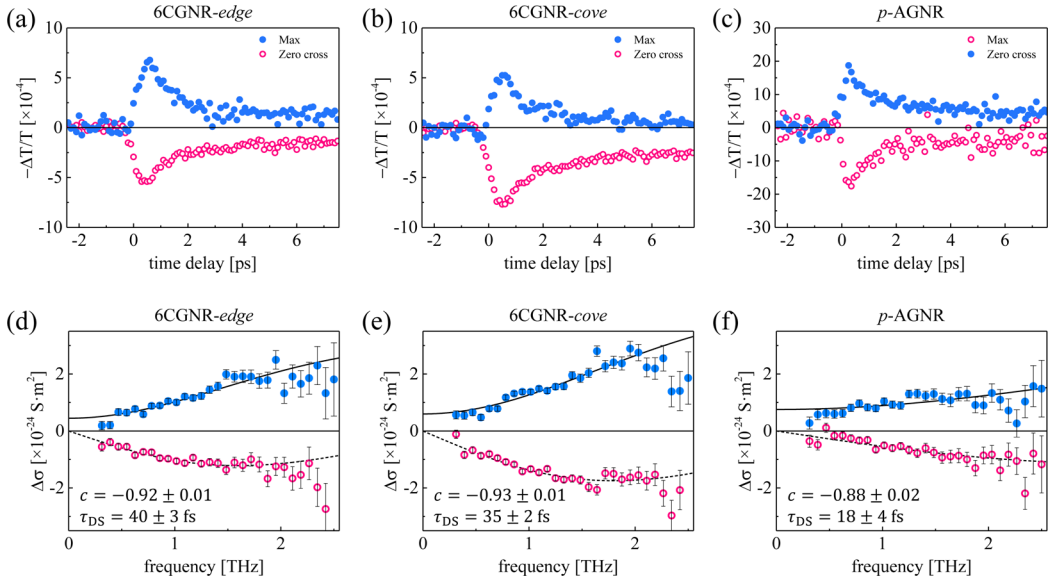

Figure 3. THz photoconductivity of GNRs dispersed in 1,2,4-trichlorobenzene, photoexcited by 400 nm pulses with a sheet excitation density N of 1.45×10^{19} photons/m^2 for 6CGNR-*edge* and -*cove* samples and 1.6×10^{19} photons/m^2 for the *p*-AGNRs. (a−c) Graphs showing the dependence of the relative change in THz field transmitted through the sample on the pump−probe delay for 6CGNR-*edge*, -*cove*, and *p*-AGNR, respectively. The blue solid circles correspond to the change at the peak field of the THz pulse (representing the dynamics in real conductivity), and the red hollow circles show the change in the crossing point of the THz field (representing a change in the imaginary part of the conductivity). (d−f) Graphs showing the complex frequency-resolved conductivity measured 0.5 ps after photoexcitation, at the peak of the photoconductivity. The conductivity is scaled to the density N of absorbed photons. The lines in (d), (e), and (f) show the results of the Drude−Smith model, with parameters shown in the respective panels.

time delays between the optical pump and arrival of the THz probe at the sample. Simultaneous scanning of the optical pump and THz detection gating laser pulses with respect to THz generation laser pulse in our setup ensures that all the points in the differential THz waveform (representing the photoinduced changes in sample conductivity) are acquired at the same optical pump−THz probe delay. The comparison of the Fourier transforms of the THz pulses interacting with the sample before and after its photoexcitation yields the complex-valued photoconductivity $\Delta\sigma(\omega)$ spectra of the sample (following the procedure described in Jensen et al.[30]): the complex-valued photoconductivity of the material at each time delay after its photoexcitation, for the frequencies ω contained in the THz probe pulses (in this experiment, in the frequency range 0.3−2.5 THz). The ac photoconductivity in the THz frequency range provides a characteristic measure of the transport properties of free charges on the nanoscale. To illustrate this, consider the $\sim 10^5$ m/s thermal velocity of an electron at room temperature, so that, in the ∼1 ps duration of a THz cycle, the motion of charges is probed on a length scale of only <100 nm.[19] As such, the conductivity is probed on length scales substantially shorter than the actual length of the nanoribbons studied here (∼100 to 100s of nm), so that the effects on the conductivity due to the ends of the ribbons can be neglected. We note that in these measurements one cannot distinguish between the conductivity contributions from electrons and holes, so that the sum of both contributions is measured simultaneously.[19]

The sub-picosecond time evolution of real and imaginary spectrally weighted, frequency-integrated photoconductivity of the sample following the photoexcitation can be obtained by measuring the attenuation of the peak THz field[32] and the change of the field in the crossing point of the probe pulse,[33] respectively. Such a transient photoconductivity dynamics of all three types of GNRs are shown as a function of pump−probe time delay in Figure 3a−c. After its initial rise, the photoconductivity shows fast (∼1 ps) decays followed by a slower decay component. Upon the initial fast decay of the signal, the imaginary conductivity remains large relative to the real conductivity. The observed negative imaginary conductivity at later times (together with the vanishingly small real part) in all GNR samples indicates that at later times after the photoexcitation the conductivity response is dominated by bound charges, such as excitons, and not by free carriers.[34] This observation is not surprising: the one-dimensional nature of GNRs provides strong quantum confinement, while the weak charge screening due to the low dielectric constant of the environment causes efficient exciton formation. We note that similar photoconductivity has been previously reported for narrower[30] and wider[16] GNRs.

In our experiments, the GNR samples have been optically excited at photon densities ranging from 0.1×10^{19} to 2.3×10^{19} photon/m^2. We have found that at high excitation densities (>∼1.3×10^{19} photon/m^2) the magnitude of the real-valued photoconductivity for all three samples deviates from the linear dependency observed at the lower fluences. This can be explained either by absorption saturation in the nanoribbons or by the increased carrier density at higher incident fluences facilitating more efficient binding of electrons and holes, i.e., formation of neutral excitons that do not contribute to the THz absorption.[35] In both scenarios, the per-photon efficiency of converting absorbed photons into mobile, free carriers is reduced at elevated excitation densities compared to lower excitation densities. In our experiments, care was therefore taken to stay in the linear excitation regime.

The frequency-resolved, complex-valued conductivity spectra (Figure 3d−f), shedding light on the nature of carrier transport, have been measured at the maxima of the photoinduced THz

DOI: 10.1021/jacs.7b03467
J. Am. Chem. Soc. 2017, 139, 7982−7988

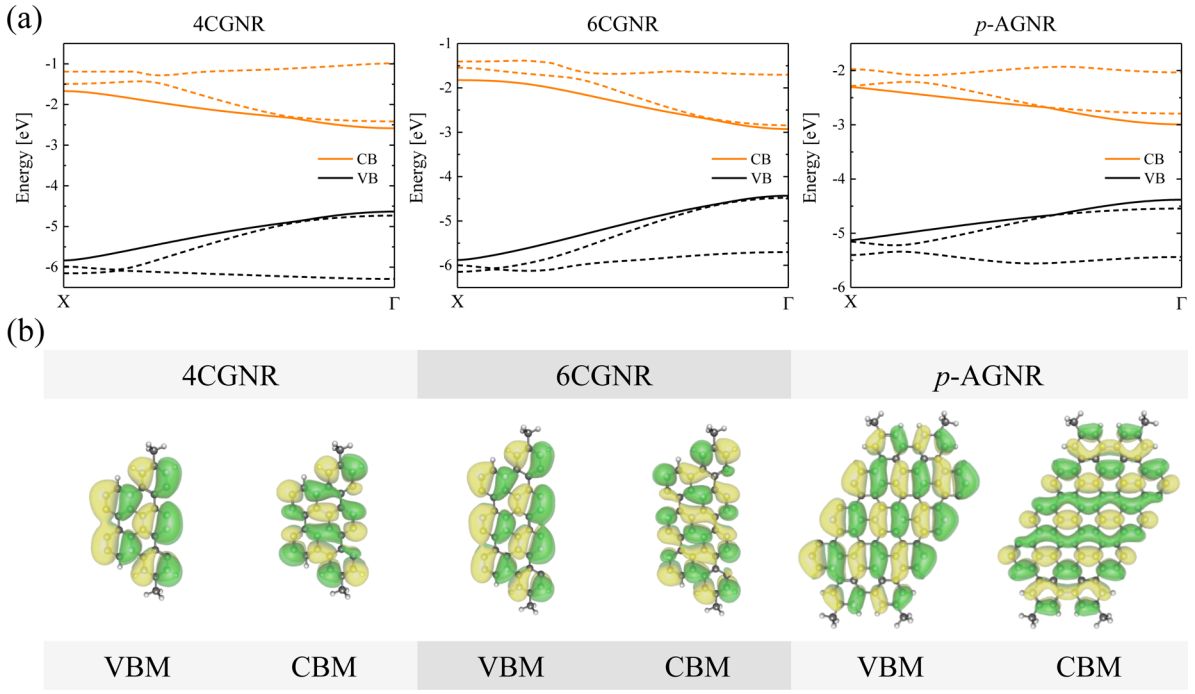

Figure 4. Electronic structure of the graphene nanoribbons studied. (a) Band structure (dashed lines) showing the frontier crystal orbitals (solid lines). (b) Plots of the wave functions at valence band maximum (VBM) and conduction band minimum (CBM), i.e., at the Γ point.

absorption, approximately 0.5 ps after optical excitation. The conductivity spectra for all GNR types are characterized by positive real and negative imaginary parts, both increasing in absolute magnitude toward higher THz frequencies. This behavior qualitatively resembles the conductivity typical for many nanometer-sized semiconductors, including narrower GNRs, carbon nanotubes,[30] and also semiconducting polymers.[36] These conductivity spectra can be well described by the Drude−Smith (DS) model.[37] The DS model applies to the conductivity by free carriers in a medium where they experience preferential backscattering on long-range potential corrugations. The use of this conductivity model can be justified by noting that other models (such as Lorentz) cannot reproduce the experimentally measured large real conductivity relative to the imaginary one. Further, a hopping model seems less appropriate for the GNRs studied here, as their structures are uniform and have minimal defects. The expression for the DS conductivity reads

$$\sigma_{DS} = \frac{\varepsilon_0 \omega_P{}^2 \tau_{DS}}{1 - i\omega\tau_{DS}}\left(1 + \frac{c}{1 - i\omega\tau_{DS}}\right) \quad (1)$$

where ε_0 is the vacuum permittivity, ω_P is the plasma frequency, τ_{DS} is the average carrier momentum scattering time, and the parameter c describes the correlation between carrier momentum before and after a scattering event. For $c = 0$, there is no correlation, and each scattering event fully randomizes the momentum, reducing eq 1 to the classical Drude model for a perfectly free electron gas. For $c = -1$, there is complete anticorrelation, i.e., complete carrier backscattering. Qualitatively, the c parameter is indicative of the carrier localization, with $c = 0$ being a perfectly free and $c = -1$ a fully localized carrier not capable of dc conduction.

The frequency-resolved conductivity spectra for all GNR samples (Figure 3d−f) can be described by the DS model (eq 1) with c parameters of −0.92 ± 0.01 (−0.93 ± 0.01) for 6CGNRs-*edge* (*-cove*) and −0.88 ± 0.02 for *p*-AGNRs samples. A very similar c parameter value has been reported for narrower 4CGNRs.[30] As shown in ref 30, these values for the c parameter are in reasonable agreement with that expected for a randomly oriented infinite 1D conductors in a nonconducting solution: the THz field is linearly polarized and can accelerate charges only in nanoribbons whose main axis is aligned along the THz field polarization. This assumption of an infinite 1D conductor can be applied for the current samples as well, where the length of the GNRs (100's of nm) is much longer than the length scale of average carrier propagation driven by the THz field.

The crucially important value obtained from fitting the THz conductivity spectra to the DS model is the carrier momentum scattering time, τ_{DS}, which is a measure of the intrinsic conductivity of the GNRs and is related to the carrier mobility $\mu = e\tau_{DS}/m^*(1 + c)$. Applying the DS model to the data, we obtain the momentum scattering times τ_{DS} equal to 40 ± 3 and 35 ± 2 fs for the 6CGNR-*edge* and *-cove* samples, respectively, and 18 ± 4 fs for the *p*-AGNRs. Both the c parameters (∼−0.92) and the scattering times (∼37 fs) are identical within experimental error for the 6CGNRs-*edge* and *-cove*, implying that the conductivity within the nanoribbon is largely unaffected by the precise placement of the alkyl chains and the induced distortion of the peripheral benzene rings. For the narrower 4CGNR, a shorter scattering time of 30 fs has previously been reported.[30] For the *p*-AGNR ribbons, the scattering time is however substantially reduced, amounting to only half of that of the 6CGNRs. The trend reveals $\tau_{DS}^{6CGNR} > \tau_{DS}^{4CGNR} > \tau_{DS}^{p\text{-}AGNR}$.

To shed light on the origin of the variation in the measured scattering rates for the different nanoribbons and the observed dependence on GNR width, we have performed electronic structure and transport calculations. The electronic structure of the graphene nanoribbons, including 4CGNR, has been calculated at the density functional theory (DFT) level using the screened exchange hybrid exchange−correlation functional

DOI: 10.1021/jacs.7b03467
J. Am. Chem. Soc. 2017, 139, 7982−7988

Table 1. Major Results of DFT Study and Carrier Transport Calculations

GNR structure	E_g (eV)	carriers	E_1 (eV)	C (eV·Å^{-1})	m^* (m_e)	μ (cm^2·V^{-1}·s^{-1})	scattering time, τ_{BTE} (fs)
4CGNR	2.056	h	5.60	202.1	0.228	472	61
		e	0.84		0.246	18 700	2615
6CGNR	1.508	h	6.28	299.6	0.154	994	87
		e	0.91		0.163	43 800	4060
p-AGNR	1.388	h	8.80	130.29	0.0847	542	26
		e	1.40		0.0838	21 800	1040

HSE06 and the standard 6-31G* basis set.[38] Note that the alkyl side chains, which should not contribute to the frontier crystal orbitals, have been ignored in the calculations (i.e., these were substituted with hydrogen atoms), even though they have a minor impact on the band structure, as can be seen from optical spectra (Figure 2). As such, the calculations do not differentiate between the 6CGNR-*edge* and -*cove* ribbons. The experimental observation that, within error, the responses of those two ribbons are indistinguishable seems to justify this approximation. Calculations were performed for *p*-AGNRs, the 6CGNRs, and their narrower counterpart 4CGNRs.

Following earlier theoretical works on various carbon nanostructures,[39−42] we have next computed the charge carrier mobility and scattering times using the semiclassical Boltzmann transport equation (BTE) while accounting for coupling of the charges to acoustic phonons. This is achieved by means of the deformation potential (DP) theory, where it is assumed that the local deformations induced by the acoustic phonons are similar to the homogeneously deformed crystal.

Except for some pathological cases (very weak or linear dispersion), the effective mass approximation provides a reasonable solution to the BTE/DP problem, with the charge carrier mobility μ expressed as

$$\mu = \frac{e\tau_{BTE}}{m^*} = \frac{e\hbar^2 C}{\sqrt{2\pi k_B T}\,|m^*|^{3/2} E_1^{\,2}} \quad (2)$$

where e is the elementary charge, τ_{BTE} the scattering time, m^* the effective mass, C the elastic constant, and E_1 the DP constant. In order to obtain C and E_1, the lattice vector of the GNR is stretched or compressed along the longitudinal axis. By fitting the total energy with respect to the lattice change, C can be derived from $\Delta E/l_0 = C(\Delta l/l_0)^2/2$. Here, l_0 is the lattice constant at equilibrium, and $\Delta\varepsilon$ and ΔE are the changes in lattice constant and total energy. The DP constant is defined as $E_1 = \Delta\varepsilon/(\Delta l/l_0)$, where $\Delta\varepsilon$ is the energy change of the corresponding band near the Fermi surface due to Δl (at valence band maximum (VBM) for holes and at conduction band minimum (CBM) for electrons). The effective mass can be calculated from the second derivative around VBM (CBM) for a hole (electron) as $m^* = \hbar[\partial^2\varepsilon(k)/\partial k^2]^{-1}$. Here, $\varepsilon(k)$ is the energy dispersion of VB and CB.

The band structure diagram of the three ribbons is displayed in Figure 4a, and the wave functions of the frontier crystal orbitals at the Γ-point are plotted in Figure 4b. The most striking feature from Figure 4a is the close resemblance between the electronic band structure of the "cove"-type (CGNR) and armchair (AGNR) ribbons: these systems feature a very similar band gap and the usual squared dependence of energy with momentum close to the band edges. This is at odds with the band dispersion expected for purely zigzag (ZGNR) ribbons displaying flat, localized, edge states around the Fermi surface,[26] whereas the CGNRs share the same crystal direction as ZGNRs. The marked difference between ZGNRs and the CGNRs can be understood in terms of Clar's theory: with the benzo-fused rings at the edges, CGNRs have a single Clar formula with a fully benzenoid structure without any unpaired electrons. In contrast, the corresponding representation of ZGNRs involves unpaired electrons confined at the ribbon edges.[43] Note that the number and relative position of the "protruding" benzo-rings in such "cove"-type GNRs, based on ZGNR cores, have a profound impact on their electronic structure and charge transport properties.

Table 1 summarizes the relevant quantities obtained from the calculation of the BTE charge carrier mobility, including the scattering times, τ_{BTE}. Irrespective of the charge carrier, we find lower τ_{BTE} values for the *p*-AGNR, which can be associated with lower elastic constant, C, and larger electron−phonon coupling, E_1, to longitudinal acoustic distortions. For all ribbons investigated, the electron scattering times are significantly larger than the corresponding hole values, which can be explained by the weaker coupling of the electrons to the phonons. This, in turn, can be understood by inspecting the wave functions shown in Figure 4b: at the VBM of all GNRs, the crystal orbitals have nodal planes running perpendicular to the ribbon direction so that stretching or compressing the ribbons implies changing the antibonding character of all carbon−carbon bonds, which hence results in a large shift in the VBM and a high E_1 value for holes. In contrast, the CBMs of the ribbons show a mixed bonding−antibonding pattern along the ribbon axis, so coupling of electrons to the longitudinal phonons is less pronounced.

These theoretical results reveal several interesting aspects of carrier mobility in nanoribbons. First of all, it is apparent that the hole scattering times derived from theory, summarized in Table 1, reproduce the experimentally observed trend: $\tau_{BTE}^{6CGNR} > \tau_{BTE}^{4CGNR} > \tau_{BTE}^{p\text{-}AGNR}$. The results further confirm that, perhaps somewhat surprisingly, there is no direct correlation between band gap and mobility: although one might expect the mobility to monotonously increase toward that of "bulk" graphene for increasingly smaller band gap, this is not the case for the nanoribbons reported here. Specifically, for the *p*-AGNR (with the lower band gap), the effective masses of electrons and holes are reduced substantially, indeed approaching the massless properties of bulk graphene, but this is more than compensated for by a reduction in scattering time, due to stronger coupling with phonons, so that the overall mobility is reduced, compared to the CGNR ribbons.

The calculated scattering times are substantially larger than those measured in the experiment, which can be traced to the fact that the calculated BTE scattering time only includes the effects of (acoustic) phonons on the motion of charge carriers. As such, the difference between the calculated and experimental scattering rates must be due to additional factors affecting scattering rates of charge carriers in graphene nanoribbons, such as alkyl side chains and structural distortions in dispersion,

DOI: 10.1021/jacs.7b03467
J. Am. Chem. Soc. 2017, 139, 7982−7988

i.e., conformational effects, which have not been included in the theory.

The scattering time inferred from the experimental data using the phenomenological DS model (τ_{DS}) is generally defined by the typical length scale of energetic corrugation relative to the mean free propagation path of the carriers.[44] In the ideal Drude model limit ($c = 0$), the electronic corrugation is negligible, and charge carriers undergo momentum-randomizing scattering events due to, for example, collisions with phonons. Therefore, τ_{DS} coincides with the average carrier momentum scattering time in the material in the absence of additional potential corrugation such as physical boundaries[44] or torsional or chemical defects. For the GNRs, the absence of such additional potential corrugation is expected to occur for the case of carriers moving along the axis of an infinite and straight, chemically perfect nanoribbon, in a perfect dielectric continuum. In such a case the scattering time is expected to equal the one calculated with BTE (τ_{BTE}). In reality the GNRs are finite, potentially flexible polymer chains floating in a dipolar molecular liquid and inevitably tend to bend, twist, and entangle/aggregate with each other. Moreover, the theory does not take into account potential scattering from the side chains of the GNRs. Besides random orientation of the ribbon's main axis (which is accounted for by the localization parameter c in the DS model) such energetic corrugations lead to reduced scattering time of the carriers.

To estimate the typical size of these possible potential corrugations, we employ a simple model that relates measured DS scattering time to the calculated BTE one. To this end, we assume a charge carrier propagating along the ribbon axis which scatters on a potential barrier (for instance a twist) after traveling over distance a. The mean scattering time for such a charge is equal to

$$\bar{\tau} = \frac{\int_0^{a/v_{therm}} t \cdot p(t)\, dt}{\int_0^{a/v_{therm}} p(t)\, dt} = \tau_{BTE}\left(1 - \frac{a}{l_{free}}\frac{1}{\exp(a/l_{free}) - 1}\right) = \tau_{DS} \quad (3)$$

where $p(t) = \exp(-t/\tau_{BTE})$ is proportional to the probability density that the carrier scatters at time t. Here $v_{therm} = \sqrt{2k_BT/m^*}$ is thermal velocity of the carriers in 2D with effective mass m^*, taken from DFT calculations, and $l_{free} = v_{therm}\tau_{BTE}$ is the carrier mean free path. Solving eq 3 gives a mean value of the distance a between consecutive scattering potentials on a GNR. The results of the simple procedure are shown in Table 2 and reveal that a lies between 10 and 20 nm for all the GNR structures. Comparing the 4CGNR to the 6CGNR, it seems that increasing the width of the nanoribbons leads to a substantial increase in the value for a. This indicates that bends and/or twists in the nanoribbon structure, which are expected to be reduced for the wider 6CGNRs, play a role in the electronic corrugation of the GNRs. As such, it would be highly desirable to develop a full theoretical model that includes the coupling of the charge carriers to local distortions induced by the edges and the solubilizing alkyl side chains, work now in progress.

Table 2. BTE and DS Carrier Scattering Times and Estimated Distance between Corrugations

GNR structure		τ_{BTE} (fs)	τ_{DS} (fs)	a (nm)
4CGNR	h	61	30[a]	15
	e	2615		12
6CGNR	h	87	35−40	22
	e	4060		18
p-AGNR	h	26	18	17
	e	1040		12

[a]The value has been taken from work by Jensen et al.[30]

CONCLUSIONS

In conclusion, the photoconductive properties of GNRs with different edge structures and side-chain functionalization appear to be qualitatively similar and can be well-explained by a conductivity model of free carriers with preferential back-scattering on long-range potential corrugations (Drude−Smith model). The carrier scattering times derived from this model suggest that the structural distortion induced by alkyl functionalization at different peripheral positions has little impact on the transport properties of GNRs, while the effect of varying the edge structure of GNR is substantial. On the basis of these and previous (4CGNR)[30] measurements, there is a clear trend: $\tau_{DS}^{6CGNR} > \tau_{DS}^{4CGNR} > \tau_{DS}^{p\text{-}AGNR}$. Theoretical DFT calculations in conjunction with Boltzmann transport equations show the same trend, but with substantially increased values for carrier scattering time. A simple model has been used to account for GNRs' corrugation as a possible origin of reduced scattering time as measured in the experiments. This simple model produces an effective mean free path of carriers in graphene nanoribbons on the order of tens of nanometers.

The results shown here demonstrate that structural distortion of the GNRs by edge functionalization with alkyl chains at different positions has minimal impact on the transport properties of the ribbons, despite the modulation of the band structure. There is, in contrast, a strong dependence of the optoelectronic properties of the ribbons on their physical and electronic structure, with a nontrivial dependence of the charge carrier mobility on ribbon width. Further studies on GNRs functionalized with electron-donating groups are planned in our laboratories.

AUTHOR INFORMATION

Corresponding Authors

*ivanov@mpip-mainz.mpg.de
*bonn@mpip-mainz.mpg.de

ORCID

Silvio Osella: 0000-0001-8541-1914
Hai I. Wang: 0000-0003-0940-3984
Akimitsu Narita: 0000-0002-3625-522X
Klaus Müllen: 0000-0001-6630-8786
Mischa Bonn: 0000-0001-6851-8453

Notes

The authors declare no competing financial interest.

ACKNOWLEDGMENTS

This work was financially supported by DFG Priority Program Graphene SPP 1459, the Max Planck Society, and the European Commission through the FET-Proactive Project "MoQuaS" (FP7-ICT-2013-10, contract number 610449), Graphene Flagship, and EU Career Integration Grant (EU CIG 334324 LIGHTER). The work in Mons has been funded by the Belgian National Fund for Scientific Research. D.B. is an FNRS Research Director.

DOI: 10.1021/jacs.7b03467
J. Am. Chem. Soc. 2017, 139, 7982−7988

REFERENCES

(1) Novoselov, K. S.; Geim, A. K.; Morozov, S. V.; Jiang, D.; Zhang, Y.; Dubonos, S. V.; Grigorieva, I. V.; Firsov, A. A. *Science* **2004**, *306* (5696), 666−669.
(2) Geim, A. K.; Novoselov, K. S. *Nat. Mater.* **2007**, *6* (3), 183−191.
(3) Bonaccorso, F.; Sun, Z.; Hasan, T.; Ferrari, A. C. *Nat. Photonics* **2010**, *4* (9), 611−622.
(4) Banszerus, L.; Schmitz, M.; Engels, S.; Dauber, J.; Oellers, M.; Haupt, F.; Watanabe, K.; Taniguchi, T.; Beschoten, B.; Stampfer, C. *Sci. Adv.* **2015**, *1* (6), e1500222.
(5) Mak, K. F.; Sfeir, M. Y.; Wu, Y.; Lui, C. H.; Misewich, J. A.; Heinz, T. F. *Phys. Rev. Lett.* **2008**, *101* (19), 196405.
(6) Mak, K. F.; Shan, J.; Heinz, T. F. *Phys. Rev. Lett.* **2011**, *106* (4), 046401.
(7) Avouris, P.; Chen, Z.; Perebeinos, V. *Nat. Nanotechnol.* **2007**, *2* (10), 605−615.
(8) Schwierz, F. *Nat. Nanotechnol.* **2010**, *5* (7), 487−496.
(9) Schwierz, F. *Proc. IEEE* **2013**, *101* (7), 1567−1584.
(10) Castro Neto, A. H.; Guinea, F.; Peres, N. M. R.; Novoselov, K. S.; Geim, A. K. *Rev. Mod. Phys.* **2009**, *81* (1), 109−162.
(11) Han, M. Y.; Özyilmaz, B.; Zhang, Y.; Kim, P. *Phys. Rev. Lett.* **2007**, *98* (20), 206805.
(12) Abbas, A. N.; Liu, G.; Liu, B.; Zhang, L.; Liu, H.; Ohlberg, D.; Wu, W.; Zhou, C. *ACS Nano* **2014**, *8* (2), 1538−1546.
(13) Jiao, L.; Zhang, L.; Wang, X.; Diankov, G.; Dai, H. *Nature* **2009**, *458* (7240), 877−880.
(14) Kosynkin, D. V.; Higginbotham, A. L.; Sinitskii, A.; Lomeda, J. R.; Dimiev, A.; Price, B. K.; Tour, J. M. *Nature* **2009**, *458* (7240), 872−876.
(15) Narita, A.; Feng, X.; Hernandez, Y.; Jensen, S. A.; Bonn, M.; Yang, H.; Verzhbitskiy, I. A.; Casiraghi, C.; Hansen, M. R.; Koch, A. H. R.; Fytas, G.; Ivasenko, O.; Li, B.; Mali, K. S.; Balandina, T.; Mahesh, S.; De Feyter, S.; Müllen, K. *Nat. Chem.* **2014**, *6* (2), 126−132.
(16) Narita, A.; Verzhbitskiy, I. A.; Frederickx, W.; Mali, K. S.; Jensen, S. A.; Hansen, M. R.; Bonn, M.; De Feyter, S.; Casiraghi, C.; Feng, X.; Müllen, K. *ACS Nano* **2014**, *8* (11), 11622−11630.
(17) Narita, A.; Wang, X.-Y.; Feng, X.; Müllen, K. *Chem. Soc. Rev.* **2015**, *44* (18), 6616−6643.
(18) Kim, W. Y.; Kim, K. S. *Nat. Nanotechnol.* **2008**, *3* (7), 408−412.
(19) Ulbricht, R.; Hendry, E.; Shan, J.; Heinz, T. F.; Bonn, M. *Rev. Mod. Phys.* **2011**, *83* (2), 543−586.
(20) Chen, Z.; Lin, Y.-M.; Rooks, M. J.; Avouris, P. *Phys. E* **2007**, *40* (2), 228−232.
(21) Bennett, P. B.; Pedramrazi, Z.; Madani, A.; Chen, Y.-C.; de Oteyza, D. G.; Chen, C.; Fischer, F. R.; Crommie, M. F.; Bokor, J. *Appl. Phys. Lett.* **2013**, *103* (25), 253114.
(22) Llinas, J. P.; Fairbrother, A.; Barin, G. B.; Shi, W.; Lee, K.; Wu, S.; Choi, B. Y.; Braganza, R.; Lear, J.; Kau, N.; Choi, W.; Chen, C.; Pedramrazi, Z.; Dumslaff, T.; Narita, A.; Feng, X.; Müllen, K.; Fischer, F.; Zettl, A.; Ruffieux, P.; Yablonovitch, E.; Crommie, M.; Fasel, R.; Bokor, J. *arXiv:1605.06730*, 2016.
(23) Celis, A.; Nair, M. N.; Taleb-Ibrahimi, A.; Conrad, E. H.; Berger, C.; de Heer, W. A.; Tejeda, A. *J. Phys. D: Appl. Phys.* **2016**, *49* (14), 143001.
(24) Lloyd-Hughes, J.; Jeon, T. I. *J. Infrared, Millimeter, Terahertz Waves*; **2012**, *33*, 871−925.
(25) Kastler, M.; Pisula, W.; Wasserfallen, D.; Pakula, T.; Müllen, K. *J. Am. Chem. Soc.* **2005**, *127* (12), 4286−4296.
(26) Osella, S.; Narita, A.; Schwab, M. G.; Hernandez, Y.; Feng, X.; Müllen, K.; Beljonne, D. *ACS Nano* **2012**, *6* (6), 5539−5548.
(27) Hu, Y.; Xie, P.; Meggendorfer, F.; Straasø, L. A.; Hansen, M. R.; De Corato, M.; Ruini, A.; Ran, W.; Simon, P.; Li, J.; Stutzmann, M.; Finley, J.; Garrido, J. A.; Molinari, E.; Feng, X.; Barth, J. V.; Palma, C. A.; Prezzi, D.; Müllen, K.; Narita, A. In preparation.
(28) Huang, Y.; Mai, Y.; Beser, U.; Teyssandier, J.; Velpula, G.; van Gorp, H.; Straasø, L. A.; Hansen, M. R.; Rizzo, D.; Casiraghi, C.; Yang, R.; Zhang, G.; Wu, D.; Zhang, F.; Yan, D.; De Feyter, S.; Müllen, K.; Feng, X. *J. Am. Chem. Soc.* **2016**, *138* (32), 10136−10139.
(29) Soavi, G.; Dal Conte, S.; Manzoni, C.; Viola, D.; Narita, A.; Hu, Y.; Feng, X.; Hohenester, U.; Molinari, E.; Prezzi, D.; Müllen, K.; Cerullo, G. *Nat. Commun.* **2016**, *7*, 11010.
(30) Jensen, S. A.; Ulbricht, R.; Narita, A.; Feng, X.; Müllen, K.; Hertel, T.; Turchinovich, D.; Bonn, M. *Nano Lett.* **2013**, *13* (12), 5925−5930.
(31) Hendry, E.; Schins, J. M.; Candeias, L. P.; Siebbeles, L. D. A.; Bonn, M. *Phys. Rev. Lett.* **2004**, *92* (19), 196601.
(32) Lui, K. P. H.; Hegmann, F. A. *Appl. Phys. Lett.* **2001**, *78* (22), 3478−3480.
(33) Wang, F.; Shan, J.; Islam, M. A.; Herman, I. P.; Bonn, M.; Heinz, T. F. *Nat. Mater.* **2006**, *5* (11), 861−864.
(34) Dressel, M.; Grüner, G. *Electrodynamics of Solids: Optical Properties of Electrons in Matter*; Cambridge University Press, 2002.
(35) Hangleiter, A.; Jin, Z.; Gerhard, M.; Kalincev, D.; Langer, T.; Bremers, H.; Rossow, U.; Koch, M.; Bonn, M.; Turchinovich, D. *Phys. Rev. B: Condens. Matter Mater. Phys.* **2015**, *92* (24), 241305.
(36) Jin, Z.; Gehrig, D.; Dyer-Smith, C.; Heilweil, E. J.; Laquai, F.; Bonn, M.; Turchinovich, D. *J. Phys. Chem. Lett.* **2014**, *5* (21), 3662−3668.
(37) Smith, N. V. *Phys. Rev. B: Condens. Matter Mater. Phys.* **2001**, *64* (15), 155106.
(38) Heyd, J.; Scuseria, G. E.; Ernzerhof, M. *J. Chem. Phys.* **2003**, *118* (18), 8207−8215.
(39) Perebeinos, V.; Tersoff, J.; Avouris, P. *Phys. Rev. Lett.* **2005**, *94* (8), 086802.
(40) Long, M.-Q.; Tang, L.; Wang, D.; Wang, L.; Shuai, Z. *J. Am. Chem. Soc.* **2009**, *131* (49), 17728−17729.
(41) Xu, H.; Heinzel, T. *J. Phys.: Condens. Matter* **2012**, *24* (45), 455303.
(42) Dugaev, V. K.; Katsnelson, M. I. *Phys. Rev. B: Condens. Matter Mater. Phys.* **2013**, *88* (23), 235432.
(43) Chen, L.; Wang, L.; Beljonne, D. *Carbon* **2014**, *77*, 868−879.
(44) Němec, H.; Kužel, P.; Sundström, V. *Phys. Rev. B: Condens. Matter Mater. Phys.* **2009**, *79* (11), 115309.

DOI: 10.1021/jacs.7b03467
J. Am. Chem. Soc. 2017, 139, 7982−7988